1 **Enhanced photodegradation of dimethoxybenzene isomers in/on ice compared to in aqueous**
2 **solution**

4 Ted Hullar[1], Theo Tran[1], Zekun Chen[2], Fernanda Bononi[2], Oliver Palmer[1,3], Davide Donadio[2], and
5 Cort Anastasio[1, *]

6 [1] Department of Land, Air and Water Resources, University of California, Davis, One Shields
7 Avenue, Davis, CA 95616, USA

8 [2] Department of Chemistry, University of California, Davis, One Shields Avenue, Davis, CA
9 95616, USA

10 [3] Now at TeraPore Technologies, 407 Cabot Road, South San Francisco, CA 94080

11 [*] Corresponding author, canastasio@ucdavis.edu, (530) 754-6095

13 **Abstract**

14 Photochemical reactions of contaminants in snow and ice can be important sinks for organic and
15 inorganic compounds deposited onto snow from the atmosphere, and sources for photoproducts
16 released from snowpacks into the atmosphere. sources and sinks for various organic and
17 inorganic compounds. Snow contaminants can be found in the bulk ice matrix, in internal liquid-
18 like regions (LLRs), or in quasi-liquid layers (QLLs) at the air-ice interface, where they can
19 readily exchange with the firn air. Some studies have reported that direct photochemical
20 reactions occur faster in LLRs and QLLs than in aqueous solution, while others have found
21 similar rates. Here, we measure the photodegradation rate constants for loss of the three
22 dimethoxybenzene isomers under varying experimental conditions, including in aqueous
23 solution, in LLRs, and at the air-ice interface of nature-identical snow. Relative to aqueous
24 solution, we find modest photodegradation enhancements (3- and 6-fold) in LLRs for two of the
25 isomers, and larger enhancements (15- to 30-fold) at the air-ice interface for all three isomers.
26 We use computational modeling to assess the impact of light absorbance changes on
27 photodegradation rate enhancements at the interface. We find small (2-5 nm) bathochromic (red)
28 absorbance shifts at the interface relative to in solution, which increases light absorption, but this
29 factor only accounts for less than 50% of the measured rate constant enhancements. The major
30 factor responsible for photodegradation rate enhancements at the air-ice interface appears to be
31 more efficient photodecay: estimated dimethoxybenzene quantum yields are 6- to 24-fold larger
32 at the interface compared to in aqueous solution and account for the majority (51-96%) of the
33 observed enhancements. Using a hypothetical model compound with an assumed Gaussian-
34 shaped absorbance peak, we find that a shift in the peak to higher or lower wavelengths can have
35 a minor to substantial impact on photodecay rate constants, depending on the original location of
36 the peak and the magnitude of the shift. Changes in other peak properties at the air-ice interface,
37 such as peak width and height (i.e., molar absorptivityabsorption coefficient) can also impact
38 rates of light absorption and direct photodecay. Our results suggest our current understanding of
39 photodegradation processes underestimates the rate at which some compounds are broken down,
40 as well as the release of photoproducts into the atmosphere.

41

1. Introduction

Snow and ice contain a wide variety of chemical compounds (Grannas et al. 2006), which can be transformed via photochemical reactions (Bartels-Rausch et al. 2014, Domine and Shepson 2002, Grannas et al. 2007). While snow and ice are comprised primarily of crystalline water ice, under environmental conditions there are also small areas of disordered water molecules that contain most of the solutes present in a snowpack (Barret et al. 2011, Bartels-Rausch et al. 2014, Bartels-Rausch et al. 2017, Grannas et al. 2007, Jacobi et al. 2004). Although the terminology used in the literature can vary, At the air-ice interface, these regions are commonly called quasi-liquid layers (QLLs), while those located at ice grain boundaries and other locations within the ice matrix are referred to as liquid-like regions (LLRs). Photochemistry can be important in snowpacks (Grannas et al. 2007), as light can penetrate tens of centimeters below the snow surface (France et al. 2011, Galbavy et al. 2007, Phillips and Simpson 2005), and chemical species can exchange with the firn air in the snowpack. Photochemical reactions are classified as either direct – where a compound absorbs sunlight and is transformed – or indirect – where a reactive species (e.g., hydroxyl radical) formed from a direct photoreaction reacts with the compound of interest.

Despite their importance, only a small number of direct photochemical reactions have been studied in/on ice, with variable and occasionally conflicting findings. Measurements of direct photodegradation rates for a number of inorganic solutes (e.g., nitrate, nitrite, and hydrogen peroxide) found the same temperature dependence in aqueous solution and LLRs, suggesting both compartments provide similar environments for chemical reactions (Chu and Anastasio 2003, Chu and Anastasio 2005, Chu and Anastasio 2007). The picture is more complicated for PAHs (polycyclic aromatic hydrocarbons). Two studies found little difference in PAH photochemistry in/on ice compared to solution: phenanthrene, pyrene, and fluoranthene had similar photodegradation rates in aqueous solution and in LLRs (Ram and Anastasio 2009), while anthracene and pyrene had similar rates in aqueous solution, LLRs, and at the air-ice inteface (QLLs) (Hullar et al. 2018). However, two other studies reported that the photodecay of anthracene and naphthalene were faster in LLRs and at the air-ice interface compared to in solution (Kahan and Donaldson 2007, Kahan et al. 2010). Harmine has also been reported to photodegrade faster at the air-ice interface (Kahan et al. 2010). Most recently, we found that guaiacol photodegradation was somewhat faster in LLRs, and considerably faster at the air ice interface, than in aqueous solution (Hullar et al. 2020).

To evaluate the possible causes of photodegradation enhancements in/on ice compared to solution, consider the variables that control the direct photodecay rate (M s^{-1}) for a chemical "C" in a given reservoir (Chu and Anastasio 2003):

$$\frac{d[C]}{dt} = - \sum_\lambda \frac{2303}{N_A} I_\lambda \, \Delta\lambda \, \Phi_{C,\lambda} \, \varepsilon_{C,\lambda} \, [C] \qquad (1)$$

where 2303 is a factor for units (1000 cm^3 L^{-1}) and for converting measurements from base 10 to base e, N_A is Avogadro's number (6.022 × 10^{23} molecules mol^{-1}), I_λ is the actinic flux at each wavelength (photons cm^{-2} s^{-1} nm^{-1}), $\Delta\lambda$ is the wavelength interval between photon flux data points (nm), $\varepsilon_{C,\lambda}$ is the molar absorption coefficient absorptivity for C (M^{-1} cm^{-1}), $\Phi_{C,\lambda}$ is the

84 quantum yield for loss of C (molecule photon^{-1}), and [C] is the concentration (M). Based on
85 equation 1, three factors could increase reaction rates in/on ice relative to solution: higher local
86 photon fluxes, a bathochromic (red) shift in molar absorption coefficient absorptivity ($\varepsilon_{C,\lambda}$)
87 towards longer wavelengths, which have greater photon fluxes, or larger quantum yields.

88 Many previous studies did not measure photon fluxes at the point of the reaction, so it is difficult
89 to accurately determine the significance of local flux differences in accounting for photodecay
90 enhancements in, or on, ice. However, measurements in different solute locations, e.g., in
91 solution, in LLRs, and at the air-ice interface, found that photon fluxes varied by less than a
92 factor of 1.5 (McFall and Anastasio 2016). In addition, in our recent work with guaiacol we
93 normalized photodecay rate constants for loss by photon flux but still saw large differences in
94 rate constants between solution, in ice, and at the air-ice interface (Hullar et al. 2020). Thus
95 local photon flux differences do not appear to a major factor in observed reaction rate
96 enhancements in/on ice.

97 Because natural solar photon fluxes increase by several orders of magnitude between 295 and
98 400 nm (Madronich and Flocke 1998), even a small shift in compound absorbance towards
99 longer wavelengths (i.e., a red, or bathochromic, shift) could substantially increase the amount of
100 sunlight absorbed by a compound, increasing its reaction rate. Several studies have measured
101 absorbance shifts for compounds in LLRs and at the air-ice interface relative to solution
102 (Corrochano et al. 2017, Heger et al. 2005, Heger and Klán 2007, Kahan and Donaldson 2010,
103 Kania et al. 2014, Krausko et al. 2015, Malongwe et al. 2016, Matykiewiczová et al. 2007).
104 Although Thethe absorbance of some compounds was the same as in aqueous solution, with
105 others showing shifts of other chemicals shifted by up to 15 nm either to the red or blue (i.e., a
106 hypsochromic shift); for several compounds concentrated in LLRs, shifts of up to 100 nm were
107 reported (Heger and Klán 2007). However, these large shifts were attributed to aggregated test
108 compounds and resulting intermolecular interactions, rather than individual molecules.
109 Unfortunately, measuring a compound's absorbance at the air-ice interface can be challenging,
110 particularly when using low concentrations representative of environmental conditions.
111 Accurate absorbance measurements typically require relatively high concentrations, which can
112 lead to aggregation on the ice surface, potentially influencing the absorption characteristics. To
113 avoid this problem, we recently used molecular modeling to estimate the absorbance shift for
114 guaiacol at the air-ice interface (Bononi et al. 2020, Hullar et al. 2020). While we did find a
115 slight bathochromic shift (5 nm), this shift explained less than 10% of the enhanced reaction
116 rates found experimentally measured at the interface.

117 Finally, an increased quantum yield at the air-ice interface could explain a faster reaction rate,
118 due to a greater fraction of absorbed photons resulting in loss photochemical reaction of the
119 chemical. Some studies suggest LLRs and solution represent similar reaction environments (Chu
120 and Anastasio 2003, Chu and Anastasio 2005, Chu and Anastasio 2007, Ram and Anastasio
121 2009), while others have found higher quantum yields at the air-ice interface (Hullar et al. 2020,
122 2018, Zhu et al. 2010). Our recent work with guaiacol (Hullar et al. 2020) found that changes in
123 the quantum yield were the dominant contributor to reaction rate differences between aqueous
124 solution, LLRs, and QLLs, with values up to 40-fold higher at the air-ice interface compared to
125 solution.

126 Taken together, previous studies show the importance of determining various factors to
127 understand the reasons for enhanced chemical reaction rates in snow and ice. In particular, our
128 recent results (Hullar et al. 2020) indicate that the direct photodecay of guaiacol is different in

129 aqueous solution, LLRs, and QLLs, and demonstrated how molecular modeling can be used to
130 assess the relative contributions of changes in light absorbance and quantum yield. Here, we
131 extend those results to three additional organic compounds chosen as model aromatics in the
132 environment: 1,2-, 1,3-, and 1,4-dimethoxybenzene (abbreviated 1,2-DMOB, 1,3-DMOB, and
133 1,4-DMOB, respectively; chemical structures given in Figure 1). DMOBs can be emitted into
134 the atmosphere by biomass burning (Smith et al. 2020). Several studies have examined the
135 direct photodegradation of DMOBs and methoxybenzene (anisole), but few have used
136 wavelengths relevant to tropospheric sunlight. At wavelengths greater than 290 nm, 1,2- and
137 1,3-DMOB have been reported to photodegrade slowly, with 1,4-DMOB loss being somewhat
138 faster (Amalric et al. 1993). 1,2-DMOB in acetonitrile forms a triplet excited state when
139 illuminated with 418 or 514 nm radiation (Schurmann and Lehnig 2000). Aqueous 1,4-DMOB
140 excited at 266 nm forms a triplet excited state, which decays to a solvated electron and a
141 relatively long-lived organic radical cation (Grabner et al. 1996, Grabner et al. 1980). Another
142 study (Tajima et al. 1999) with 266 nm excitation under acidic conditions (pH = 1.46) found
143 electron transfer from the excited triplet state to a hydronium ion. Although 1,2-DMOB was
144 reported to be photostable in aqueous solution when illuminated with 254 nm light (Wan and Wu
145 1990), in aqueous sulfuric acid (pH < 2) all three isomers are photoprotonated in the singlet
146 excited state. Illuminated 1,2-DMOB additionally can undergo an acid-catalyzed *ipso*
147 substitution of the alkoxy group by water, but this was not observed with the other two isomers
148 (Mosi et al. 1995, Pollard et al. 1993, Wan and Wu 1990, Zhang et al. 1994).

149 Here, wWe measure the direct photochemical reaction rate constants for loss of the three DMOB
150 isomersthese compounds in aqueous solution, LLRs, and QLLs, normalizing each to the
151 measured photon flux for a given sample type. To assess the contribution of absorbance shifts,
152 we model DMOB absorbance in aqueous solution and on an ice surface. As with guaiacol, the
153 DMOBs are all doubly-substituted aromatic rings; however, the hydroxyl group of guaiacol is
154 replaced by a methoxy group, eliminating the possible unwanted reaction with triplet excited
155 states ($^3C^*$). Further, the three isomers provide the opportunity to examine how structural
156 differences can influence light absorption, quantum yields, and ultimately photochemical
157 reactivity. To more broadly examine the importance of changes in light absorption on
158 photodecay, we also quantify how changes in the absorbance peak location, maximum
159 absorbance, and absorption peak shape affect photochemical reaction rate constants and
160 lifetimes.

161

162 **2 Methods**

163 **2.1 Materials**

164 1,2-, 1,3-, and 1,4-DMOB (99, >98, and 99% purity, respectively) were from Aldrich.
165 Acetonitrile (HPLC grade) was from Acros. 2-nitrobenzaldehyde (2NB, 98%) was from Sigma-
166 Aldrich. High purity water ("MQ") was from house-produced reverse osmosis water run through
167 a Barnstead International DO813 activated carbon cartridge and a Millipore Milli-Q Advantage
168 A10 system ($\geq$ 18.2 MΩ cm).

169 **2.2 Sample preparation**

We placed samples in 10-ml glass beakers (Pyrex) and covered them with nylon film (McMaster-Carr, approximately 25 µm thick, secured in place with an o-ring) to reduce evaporation and contamination while allowing sample illumination. ~~As discussed in our previous work with guaiacol (Hullar et al. 2020), we~~ We prepared samples using one of five different methods: 1) in an aqueous solution, where we dissolved the test compound in MQ water to give a final concentration of 1.0 µM, then we placed 10 ml of solution in a beaker and covered. 2) Freezer frozen solution, prepared identically to aqueous solution, then placed in a laboratory freezer (-20 °C) for at least 3 hours. 3) Liquid nitrogen frozen solution, which we prepared identically to aqueous solution, then placed it in a pan filled to a depth of 2 cm with liquid nitrogen; sample freezing took approximately 90 seconds. 4) Vapor deposition of gas-phase test compound to the surface of ice, where ~~Following an approach previously described (Hullar et al. 2020, Hullar et al. 2018),~~ we placed 10 ml of MQ water in a beaker, covered it with film, and froze it in a laboratory freezer. We removed and uncovered the frozen samples, and directed a nitrogen stream containing gas-phase dimethoxybenzene at the ice surface for 15 or 30 s. We then recovered the samples and placed them back in a laboratory freezer. 5) Vapor deposited to nature-identical snow, ~~which was produced as described in our previous work (Hullar et al. 2020). To deposit dimethoxybenzene onto the snow,~~ where we passed nitrogen from a tank in the cold room first through 500 ml of laboratory-made snow (to condition the nitrogen stream with water vapor), then through a glass container holding 0.4 g of DMOB, and then through a 500- or 1000-ml HDPE bottle holding the snow to be illuminated. 1,2-DMOB is a liquid at room temperature but a solid at -20 °C, while 1,3-DMOB is a liquid at both temperatures and 1,4-DMOB a solid; vapor pressures at 25 °C are 0.057, 0.030, and 0.021 kPa, respectively (USEPA 2021). We then gently mixed the treated snow and transferred it to beakers, tamped it down 10 mm below the top edge of the beaker, and covered it with nylon film. Additional details for these sample preparation methods can be found in Supplemental Section S2 and our previous works ~~As discussed in our previous work with guaiacol (Hullar et al. 2020), weFollowing an approach previously described (Hullar et al. 2020, Hullar et al. 2018),~~

2.3 Sample illumination, actinometry, and chemical analysis

Sample illumination followed the method described previously (Hullar et al. 2020). We set sample beakers upright in a drilled aluminum block set within a temperature-controlled chamber; dark samples were completely covered with aluminum foil and placed in the aluminum block next to the illuminated samples. The samples were held at 5 °C (for aqueous) or -10 °C (for ice and snow). The light source was a 1000 W Xenon arc lamp filtered with an AM1.5 airmass filter (Sciencetech) and a 295-nm longpass filter (Andover Corporation) to approximate polar sunlight and a 400-nm shortpass filter (Andover Corporation) to reduce sample heating.

After illumination, we melted the frozen samples and measured DMOB concentration using a Shimadzu HPLC (Hullar et al. 2018) with an eluent of 60:40 acetonitrile:MQ water, a flow rate of 0.70 ml min^{-1}, and detection wavelengths of 274, 273, and 287 nm for 1,2-, 1,3-, and 1,4-DMOB, respectively.

To account for differing photon fluxes across samples types and experiment days, we used 2-nitrobenzaldehyde (2NB) as a chemical actinometer (Galbavy et al. 2010, Hullar et al. 2020, Hullar et al. 2018). Except for snow samples, we prepared 10 µM 2NB actinometry samples on each experiment day using the same sample preparation and experiment treatment as the test

214 compound illuminations, although the illumination times were shorter. For snow samples, daily
215 j_{2NB} was determined by measuring j_{2NB} in aqueous solution and correcting by a previously
216 determined ratio ($j_{2NB,snow}$ / $j_{2NB,aq}$ ± 1 σ = 0.38 ± 0.015), as described in earlier work (Hullar et
217 al. 2020).

218 We used TUV (Madronich and Flocke 1998) to model spectral actinic fluxes for Summit,
219 Greenland at noon on the summer solstice (subsequently referred to "Summit conditions"). We
220 used default settings (option 1) except for wavelength interval = 0.1 nm, latitude = 72.6 degrees,
221 ground surface elevation = 3,200 m, simulation elevation = 3,200 m, total column ozone = 308
222 Dobson units, surface albedo = 0.93, and four radiative transfer streams. Using methods
223 described previously (Hullar et al. 2020), we calculated laboratory photon fluxes at 1 nm
224 intervals from measured wavelength-dependent relative light intensities and our j_{2NB} values, then
225 interpolated those fluxes to 0.1 nm resolution.

226 **2.4 Determining rate constants and quantum yields for DMOB loss**

227 We determined DMOB photodegradation rate constants for loss using the same approach used
228 for guaiacol and PAHs (Hullar et al. 2020, Hullar et al. 2018). We illuminated samples with
229 simulated polar sunlight, periodically removing a beaker (and corresponding dark beaker) for
230 analysis. To determine the photodegradation rate constant for loss, we first calculated the natural
231 logarithm of the ratio of the DMOB concentration at time t to the initial DMOB concentration,
232 then adjusted these ratios by a correction factor (Supplemental Table S1) to account for
233 differences in photon flux at each sample position (Hullar et al. 2020, Hullar et al. 2018). The
234 linear regression slope of illuminated samples gives the pseudo-first-order rate constant for loss
235 during illumination, j_{DMOB}; for dark controls, we get the rate constant for dark loss, $k'_{DMOB,dark}$.
236 To calculate the net loss attributable to photodegradation, we subtracted $k'_{DMOB,dark}$ from j_{DMOB} to
237 give the dark-corrected experimental photodegradation rate constant $j_{DMOB,exp}$. We then
238 normalized this value for the experimental photon flux by dividing $j_{DMOB,exp}$ by the daily
239 measured j_{2NB} value to give the photon flux-normalized photodegradation rate constant for loss,
240 j^*_{DMOB}. Full equations are given in our previous work [14,18].

241 We calculated quantum yields for each DMOB using methods described previously (Hullar et al.
242 2020). In short, the quantum yield was ~~determined~~ estimated for each DMOB by dividing the
243 dark-corrected experimental photodegradation rate constant ($j_{DMOB,exp}$) by the measured aqueous
244 molar absorption coefficient ~~absorptivity~~ ($\varepsilon_{DMOB,\lambda}$) and the calculated photon flux in our
245 experimental system. We determined aqueous solution molar absorption coefficients
246 ~~absorptivities~~ for each DMOB ($\varepsilon_{DMOB,\lambda}$, Supplemental Table S2) by measuring absorbance
247 spectra in five solutions (10-1000 μM) at 25 °C using a UV-2501PC spectrophotometer
248 (Shimadzu) in 1.0 cm cuvettes against a MQ reference cell. The calculated quantum yields are
249 an average value over the ranges of 250-317, 250-315, and 250-341 nm for 1,2-, 1,3-, and 1,4-
250 DMOB, respectively. We chose the low end of this range because it represents a rough natural
251 minimum of light absorbance for the three compounds and does not have any photon flux for
252 either Summit conditions or in our experimental system; the upper cutoff varies for each
253 compound and is the wavelength above which the molar absorption coefficient ~~absorptivity~~ is
254 less than 5×10^{-5} M^{-1} cm^{-1}. Based on light absorption spectra for the three compounds
255 (discussed in the results section), the wavelengths driving photodegradation in our experiments
256 are 270-300, 270-310, and 280-310 nm for 1,2-, 1,3-, and 1,4-DMOB, respectively. We
257 estimated molar absorption coefficients ~~absorptivities~~ at the air-ice interface by applying the

258 results of the computational modeling to the measured aqueous molar absorption
259 coefficients, as described in the results section below.

260 **2.5 Computational methods**

261 To investigate possible shifts in light absorbance at the air-ice interface for the three
262 dimethoxybenzene isomers, we used a multimodel approach that combines classical and first-
263 principles molecular dynamics (FPMD) simulations, excited state calculations using time-
264 dependent density functional theory (TDDFT), and machine learning (ML) (Bononi et al. 2020,
265 Tibshirani 2011).

266 As in our recent work on phenol and guaiacol, models of DMOB in aqueous solutions and at the
267 ice surface were equilibrated in classical MD simulations using the OPLS forcefield and the
268 TIP4P/ice water model (Abascal et al. 2005). To model the air-ice interface we utilized an ice
269 slab model, which captures a well-equilibrated surface structure and reproduces recent
270 measurements for QLLs (Kling et al. 2018, Sanchez et al. 2017). We then performed FPMD
271 simulations of the DMOB isomers in solution at 27 °C and at the air–ice interface at -10 °C.
272 Density functional theory (DFT)-based FPMD simulations were run using the Perdew-Burke-
273 Ernzerhof exchange and correlation functional with D3 van der Waals corrections, a double-Z
274 valence polarizable basis set for valence states and norm-conserving pseudopotentials for the
275 core states and the nuclei, as implemented in the CP2K code (Grimme et al. 2010, Hartwigsen et
276 al. 1998, Perdew et al. 1996, VandeVondele et al. 2005). For each 50 ps FPMD simulation
277 trajectory, we extracted approximately 200 statistically independent frames, replaced the
278 explicit water molecules with the self-consistent continuum solvation scheme (Timrov et al.
279 2015), and finally computed absorption spectra for each frame using TDDFT as implemented in
280 the Quantum-Espresso package (Casida et al. 2009, Giannozzi et al. 2017, Rocca et al. 2008).
281 To account for the configurational sampling at finite temperature in the specific solvation
282 environment, we computed the final spectra by ensemble averaging the 200 single frame
283 calculations for each isomer (Ge et al. 2015, Timrov et al. 2016).

284 As a refinement to our former approach, we developed a universal ML model to predict the
285 absorption spectra for all three DMOB isomers. To accomplish the transferability, we adopted a
286 more sophisticated atomic descriptor - the Bispectrum Component (BC) (Bartok et al. 2013,
287 Thompson et al. 2015). BC describes each molecule's atomic environment by projecting the
288 weighted atomic densities to four-dimensional hyperspherical harmonics, and it has been
289 previously applied to ML interatomic potential development and material property predictions
290 (Cusentino et al. 2020, Legrain et al. 2017). By using BC with the least absolute shrinkage and
291 selection operator (LASSO) regression model (Tibshirani 2011), we attain a more precise
292 estimate of the low-energy, long-wavelength tails of the spectra, which are important for
293 calculating rates of photon absorption since the photon flux is increasing in this region. To
294 assess the relative contributions of the phenyl ring and methoxy groups to the light absorbance of
295 each DMOB isomer, we decomposed the predicted peak wavelength from over $\sim$5000 frames of
296 each FPMD trajectory, with $\lambda_0 \approx 586$ nm fitted as the intercept of the ML model. Further details
297 about the simulation procedures and parameters to compute BC and analysis of excitation energy
298 predictions from the LASSO model are available Supplemental Section S1.

299 **3. Results**

300

3.1. DMOB photodegradation for each sample preparation method

321 We prepared samples using one of several methods designed to place the DMOB isomer into
322 aqueous solution, LLRs, or at the air-ice interface (sections 2.2 and 2.3). Then, we illuminated
323 the samples, periodically removing them for analysis. Supplemental Figures S1 through S12
324 show the results for every illumination experiment, with each data point representing one sample
325 beaker. Generally, dark controls show slight loss of DMOB, probably attributable to
326 volatilization; illuminated samples often show considerably greater loss due to photodegradation,
327 but the extent of loss depends on DMOB isomer and sample preparation method. Figure 1
328 summarizes the experimental results for each of the three DMOBs in aqueous solution and the
329 various frozen sample preparations. As described above, we divided each dark-corrected,
330 measured rate constant for DMOB loss by the corresponding measured j_{2NB} value to compensate
331 for the different photon fluxes in each experiment, then calculated the average photon-flux-
332 normalized rate constant ($j*_{DMOB}$) for each sample treatment; error bars in Figure 1 are the 95%
333 confidence interval of mean $j*_{DMOB}$ values.
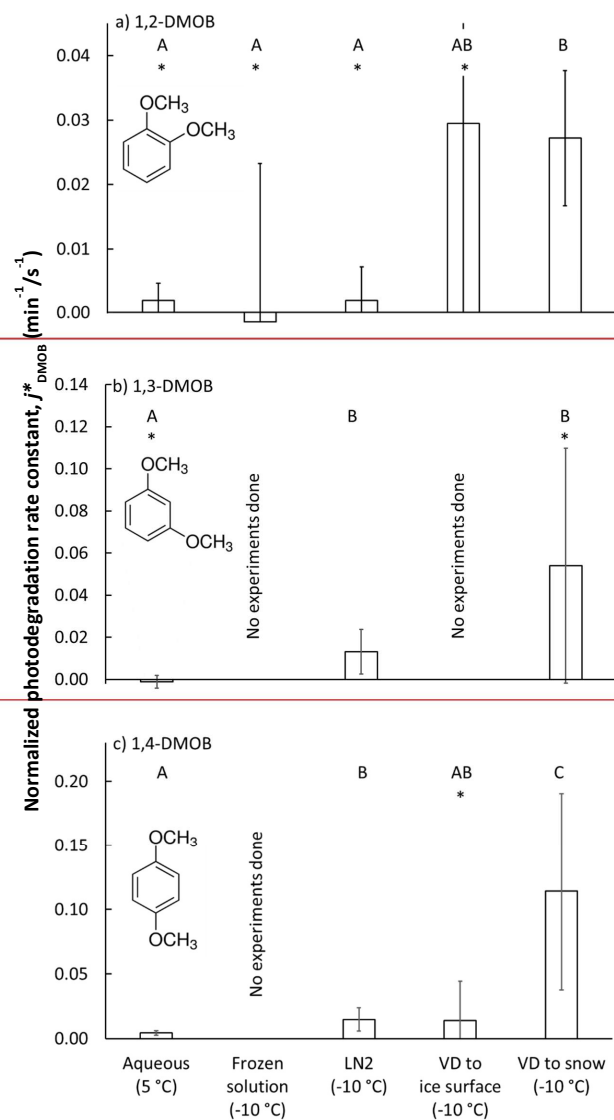
Figure 1. Photon-flux-normalized photodegradation rate constants for loss for each dimethoxybenzene isomer ($j*_{DMOB}$) under five experimental conditions: i) aqueous solution, ii) solution frozen in a laboratory

340 freezer ("Frozen solution"), iii) solution frozen in liquid nitrogen ("LN2"), iv) vapor-deposited DMOB to
341 a water ice surface ("VD to ice surface"), and v) vapor-deposited DMOB to nature-identical snow ("VD
342 to snow"). We illuminated samples at 5 °C (aqueous samples) or -10 °C (all others). Bars indicate the
343 mean value for each sample preparation method (n = 3 - 8), with error bars as 95% upper and lower
344 confidence limits of the mean (UCL and LCL). For each isomer, sample types having statistically
345 indistinguishable average rate constants as determined by a Tukey-Kramer test ($P < 0.05$) are labeled with
346 the same capital letter ("A", "B", or "C"); sample types with different letters have statistically different
347 means. For example, "AB" indicates that the average rate constant for VD to ice surface is statistically
348 indistinguishable from results labeled A or B. An asterisk ("*") indicates the average rate constant is
349 indistinguishable from zero.
350

351 As shown in Figure 1a, the 1,2-DMOB photodegradation rate in aqueous solution is slow and the
352 normalized rate constant for loss is statistically indistinguishable from zero. For frozen solution
353 experiments, the average rate constant was negative, and the data was quite noisy. Samples
354 frozen with liquid nitrogen ("LN2") should, like freezer-frozen samples, place solutes primarily
355 in internal LLRs. However, the variability in 1,2-DMOB LN2 experiments is considerably less
356 than for freezer frozen experiments, and the rate constant is roughly equivalent to that
357 determined for aqueous solution. Previous work (Hullar and Anastasio 2016) suggests more
358 homogeneous solute distribution in LN2 samples compared to frozen solution samples, which
359 may explain the reduced experimental variability in LN2 samples. The reduced variability might
360 also be due to the fact that freezing in LN2 is fast (less than 90 seconds), which reduces the time
361 available for the DMOB to react as solutes concentrate during freezing; in contrast, the freezer
362 requires much more time (typically several hours) to make ice, which can lead to more, and more
363 variable, DMOB loss. For both frozen solution and LN2 treatments, the rate constants are
364 indistinguishable from zero. The two treatment methods which put 1,2-DMOB at the air-ice
365 interface, VD to ice and VD to snow, both show normalized rate constants for loss
366 approximately 15 times faster than in aqueous solution or in LLRs. However, while
367 experimental results for the VD-to-ice treatment are highly variable (with an average rate
368 constant indistinguishable from zero), VD-to-snow experiments are more reproducible and give a
369 normalized rate constant statistically greater than zero, showing the advantage of using nature-
370 identical snow to study photodegradation at the air-ice interface. As discussed previously
371 (Hullar et al. 2020), the specific surface area (SSA) for our VD-to-snow samples (approximately
372 600 cm^2/cm^3) is much higher than in VD-to-ice samples (0.3 cm^2/cm^3). This should reduce
373 DMOB aggregation and allow chemicals to deposit more evenly, potentially explaining the
374 better experimental results from the VD-to-snow samples. For our range of measured aqueous
375 concentrations in melted VD-to-ice samples, we estimate the DMOB surface coverage at 1.7 –
376 110 monolayers. For the VD-to-snow samples, DMOB surface coverage is 0.00036 to 0.047
377 monolayers, suggesting compounds are widely dispersed and less likely to aggregate. However,
378 we cannot rule out the possibility that some of our vapor-deposited test compound is present as
379 aggregated areas of concentrated or pure compound at the snow or ice surface.

380 1,3-DMOB results are summarized in Figure 1b. Because the frozen solution and VD-to-ice
381 experiments were very noisy for 1,2-DMOB, we did not run experiments with these sample
382 treatments for 1,3-DMOB. For aqueous solution, the 1,3-DMOB average rate constant for loss is
383 slightly negative and indistinguishable from zero. In LLRs (LN2 sample treatment), 1,3-DMOB
384 photodegrades at a moderate rate, statistically greater than zero. Finally, at the air-ice interface

(VD to snow samples), the photodegradation rate constant is approximately four times faster than in LLRs, although statistically indistinguishable from zero because of very high variability.

For 1,4-DMOB in aqueous solution (Figure 1c), the average photodegradation rate is slow, but statistically greater than zero. As with 1,3-DMOB, we did not run experiments in frozen solution for 1,4-DMOB; however, LN2 experiments, which should also place solutes primarily in LLRs, showed photodecay rates both statistically greater than zero and approximately 3-fold faster than in aqueous solution. Measured VD-to-ice rates were variable, and although the average normalized rate constant for loss was similar to LN2, it was not statistically different than zero. As with 1,2-DMOB, the average 1,4-DMOB photodegradation rate constant at the air-ice interface (VD-to-snow experiments) is considerably faster than in either aqueous or LLR compartments, with a 26-fold enhancement relative to aqueous solution, and is statistically greater than zero.

To determine if the various sample treatment rate constants are statistically different from each other, we used the Tukey-Kramer test for multiple comparisons ($P < 0.05$) to generate statistical groupings, identified by the letters A, B, and C on Figures 1a-c. For 1,2-DMOB, mean rate constants for loss (j^*_{DMOB}) for aqueous, frozen solution, and LN2 samples were indistinguishable from each other. However, VD to snow gave a rate constant significantly greater than these three sample types. Because of its high experimental variability, VD to ice could not be distinguished from any of the other sample treatments. For 1,3-DMOB, aqueous samples were statistically different than both LN2 and VD to snow samples. However, LN2 and VD-to-snow samples could not be distinguished from each other. For 1,4-DMOB, VD-to-snow samples were statistically higher than every other sample type. VD-to-ice samples were indistinguishable from both aqueous and LN2 samples, although LN2 samples were statistically different, and higher, than the aqueous samples.

Table 1 presents the rate constant enhancements for each frozen sample type relative to aqueous solution; Supplemental Table S3 provides details for the various measured and computed experimental parameters. For 1,2-DMOB, photodegradation proceeds at approximately the same rate in LLRs and aqueous solution, but roughly 15-fold ($\pm$ 9.5, 1σ) faster at the air-ice interface. Because the average aqueous rate constant for 1,3-DMOB was negative, we calculated an upper-bound estimate (average + 95% UCL of the mean) for the rate constant and determined enhancements relative to that value. Compared to the aqueous rate constant for loss, we estimate the 1,3-DMOB rate constant in LLRs to be at least 6.9-fold faster, and at least 29-fold faster at the air-ice interface. Finally, for 1,4-DMOB, enhancement in LLRs is 3.4-fold ($\pm$ 2.4), and 26-fold ($\pm$ 27) at the air-ice interface. As noted in previous work (Hullar et al. 2020), vapor depositing a test compound to nature-identical snow rather than to an ice pellet surface is more representative of environmental conditions and gives more reliable experimental results, probably due to the much greater SSA of the snow. Although the experimental data show considerable variability, our results suggest DMOB photodegradation rate constants for loss are somewhat faster in LLRs than in corresponding aqueous solution, and considerably faster at the air-ice interface; this finding is similar to previously reported results with guaiacol (Hullar et al. 2020) and several other organic compounds (2007, Kahan et al. 2010, Kahan et al. 2010). Taken together with earlier work, our results here suggest that at least for some compounds, aqueous solution, LLRs, and the air-ice-interface can be different environments for photochemical reactivity.

Table 1. Summary statistics for each experimental preparation method[a]

	nᵇ	j^*_{DMOB} [c]	Enhancement[d]	Quantum Yield (Φ_{DMOB})[e]	Compart-ment[g]	$j_{TUV, DMOB}$ [h]	Lifetime[i]
		(min⁻¹/s⁻¹)	($j^*_{DMOB, i}$ / $j^*_{DMOB, aq}$)	(mlc photon⁻¹)		(s⁻¹)	(d)
1,2-DMOB							
Aqueous solution	3	0.0019 ± 0.0011	1	0.015 ± 0.0085	Aqueous	(5.0 ± 2.9) × 10⁻¹⁰	23000 ± 13000
Freezer frozen solution	3	-0.0010 ± 0.0099	-0.79 ± -5.3	-0.012 ± 0.078			
Liquid nitrogen frozen solution	4	0.0019 ± 0.0030	1 ± 1.9	0.015 ± 0.027	LLR	(5.1 ± 9.0) × 10⁻¹⁰	23000 ± 41000
Vapor-deposited to ice surface	3	0.029 ± 0.022	16 ± 15	0.13 ± 0.10			
Vapor-deposited to snow	5	0.027 ± 0.0084	15 ± 9.5	0.12 ± 0.039	QLL	(6.3 ± 1.9) × 10⁻⁹	1800 ± 570
1,3-DMOB							
Aqueous solution	6	-0.0011 ± 0.0029	1 [f]	< 0.016	Aqueous	< 2.6 × 10⁻¹⁰ʲ	> 45000ʲ
Freezer frozen solution	0						
Liquid nitrogen frozen solution	3	0.013 ± 0.0042	> 6.9	0.11 ± 0.035	LLR	(1.8 ± 1.4) × 10⁻⁹	6400 ± 5100
Vapor-deposited to ice surface	0						
Vapor-deposited to snow	5	0.054 ± 0.045	> 29	0.085 ± 0.070	QLL	(2.4 ± 2.5) × 10⁻⁷	48 ± 50
1,4-DMOB							
Aqueous solution	3	0.0043 ± 0.00073	1	0.0020 ± 0.00042	Aqueous	(1.6 ± 0.34) × 10⁻⁷	70 ± 14
Freezer frozen solution	0						
Liquid nitrogen frozen solution	3	0.015 ± 0.0036	3.4 ± 2.4	0.0075 ± 0.0018	LLR	(6.0 ± 1.5) × 10⁻⁷	19 ± 4.7
Vapor-deposited to ice surface	5	0.014 ± 0.025	3.2 ± 6.1	0.0064 ± 0.011			
Vapor-deposited to snow	8	0.11 ± 0.091	26 ± 27	0.052 ± 0.042	QLL	(4.4 ± 3.5) × 10⁻⁶	2.7 ± 2.1

The headers span: "Experimental results" covers nᵇ, j^*_{DMOB}, Enhancement, Quantum Yield; "Summit conditions estimates" covers Compartment, $j_{TUV, DMOB}$, Lifetime.

[a] Samples were held at 5 °C (aqueous samples) or -10 °C (all other preparations).

[b] Number of experiments.

[c] Listed j^*_{DMOB} values (photon-flux normalized photodegradation rate constants for loss) are means ± 1 standard deviation.

[d] Enhancement factors are the ratio of the mean j^*_{DMOB} value for each preparation method to the mean aqueous j^*_{DMOB} value for that light condition, ± the propagated standard deviation.

[e] Quantum yields are calculated individually for each experiment using the measured $j_{DMOB,exp}$ and j_{2NB}. Uncertainties for quantum yields are ± 1 standard deviation.

[f] To calculate enhancement factors, we first estimated the upper bound j^*_{DMOB} value for aqueous solution as the mean + the 95% UCL, 0.00190 min^{-1}/s^{-1}. Then, we calculated enhancement factors relative to this value.

[g] For purposes of calculating $j^*_{TUV,DMOB}$ and photochemical lifetimes, quantum yields in aqueous, LLR, and QLL compartments were assumed to be represented by aqueous solution, liquid nitrogen frozen solution, and vapor-deposited to snow sample types respectively.
[h] Listed $j^*_{TUV,DMOB}$ values (calculated photodegradation rate constants for Summit, Greenland) are means ± 1 propagated standard deviation.

[i] Photochemical lifetimes are 1 / $j^*_{TUV,DMOB}$ values ± 1 propagated standard deviation.

[j] $j^*_{TUV,DMOB}$ and photochemical lifetime calculated from upper-bound estimate of 1,3-DMOB quantum yield.

429

430

3.23 DMOB light absorbance, quantum yields, and environmental lifetimes in solution and at
the air-ice interface

Figure 2 presents the wavelength-dependent molar ~~absorptivities~~ absorption coefficients for 1,2-,
1,3-, and 1,4-DMOB, as well as guaiacol (which was studied in our previous work (Hullar et al.
2020)). 1,2- and 1,3-DMOB in solution have nearly identical absorbance curves, with maximum
absorbance at 274 and 273 nm, respectively. While guaiacol absorbs less strongly, its curve
shape and peak location are similar to 1,2- and 1,3-DMOB. In contrast, 1,4-DMOB absorbs at
longer wavelengths, with a peak absorbance at 287 nm. For comparison, the two black lines in
Figure 2 show the photon flux of our experimental system (dashed line) and the modeled actinic
flux for Summit conditions (solid line); a more detailed graph is shown in Supplemental Figure
S13. While the actinic flux at Summit starts at approximately 297 nm and increases quickly with
increasing wavelength, the experimental flux begins earlier (roughly 280 nm) and increases more
gradually. 1,2- and 1,3-DMOB in solution absorb small amounts of light under our illumination
conditions and virtually none in the Arctic environment. In contrast, the 1,4-DMOB absorbance
curve has substantial overlap with both photon flux curves and therefore absorbs light under both
experimental and natural conditions.
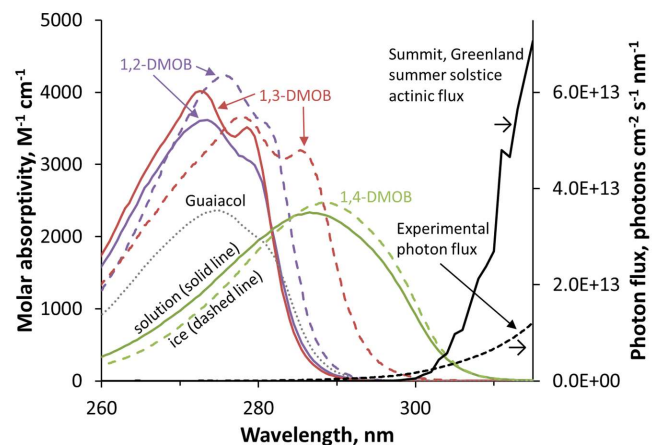
Figure 2. Light absorption spectra for the dimethoxybenzene (DMOB) isomers and guaiacol, along with
photon fluxes in our experiments and for Arctic summer conditions. Solid colored lines are the measured
molar ~~absorptivities~~ absorption coefficients for each DMOB isomer, while colored dashed lines are
predicted absorbance spectra at the air-ice interface, estimated using the results of our molecular
modeling. The solution guaiacol spectrum (dotted grey line) is provided for comparison to previous work
(Hullar et al. 2020). Black lines (right axis) represent the modeled actinic flux for Summit conditions
(solid line), and the photon flux measured in our laboratory illumination system (dashed line).

457 While we can measure light absorption by the DMOB isomers in solution, we also want to
458 understand their absorption at the air-ice interface. To estimate this, we use molecular modeling
459 combined with machine learning for each compound in aqueous solution and at the air-ice
460 interface; these modeled curves are shown in Figure 3. As shown in Supplemental Figure S14,
461 modeled absorbance bands for aqueous DMOBs peak at longer wavelengths (7 to 21 nm)
462 compared to measurements, equal to or greater than the 7 nm difference we observed for
463 guaiacol (Bononi et al. 2020, Hullar et al. 2020). These differences are caused by systematic
464 underestimation in our simulations, which is a known limitation of TDDFT calculations; the
465 peak wavelength offset relative to measured spectra tends to increase with larger molecules
466 (Leang et al. 2012, Miura et al. 2007), consistent with the greater difference here for the DMOB
467 isomers compared to our previous work with guaiacol. These differences can be corrected by
468 applying the same shifts to both solution and ice spectra (Ge et al. 2015).
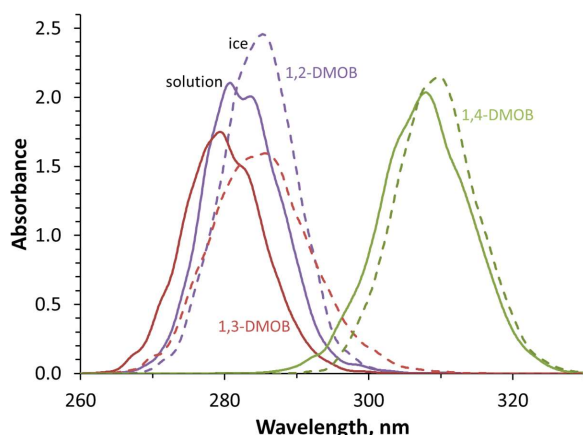
469
470
471 **Figure 3.** Modeled absorbance spectra in aqueous solution (solid lines) and at the air-ice interface (dashed
472 lines) for each DMOB isomer. Absolute absorbance values are arbitrary, but accurately reflect the
473 relative absorbance differences between isomers and conditions. Temperatures were 27 °C for aqueous
474 solution and -10 °C at the air-ice interface.
475

476 While the modeling does not accurately reproduce the absolute wavelengths of absorbance, it
477 provides useful insights into the differences between absorbance in aqueous solution and at the
478 air-ice interface. We note that a similar modeling approach comparing phenol absorbance in gas
479 and aqueous phases successfully predicted the experimentally observed ~9 nm solvatochromic
480 peak shift, as well as accurately reproducing the aqueous absorbance curve shape (Bononi et al.
481 2020). To predict the absorbance spectrum for each DMOB at the air-ice interface, we first
482 examine how the model predicts the absorbance changes from aqueous to air-ice interface, then
483 apply this change to the measured aqueous spectrum. We quantify how absorbance for a given
484 DMOB changes from aqueous to ice using three characteristics – peak location, maximum peak
485 height, and the full width of the peak at half maximum height (FWHM). In terms of the first
486 characteristic, all three compounds showed a bathochromic (red) shift at the air-ice interface

487   relative to aqueous solution; shifts were 2.4, 5.2, and 1.6 nm for 1,2-, 1,3-, and 1,4-DMOB,
488   respectively. These results are consistent with a 5-nm red shift modeled for guaiacol (Hullar et
489   al. 2020) and previous observations of anisole showing a 4-nm red shift at the air-ice interface
490   (Malongwe et al. 2016), but less than the 10-15 nm red shifts observed for three aniline
491   derivatives (Corrochano et al. 2017). For peak height, modeled absorbance peaks of 1,2- and
492   1,4-DMOB were higher at the air-ice interface compared to in solution, by 17 and 6%
493   respectively, while the 1,3-DMOB peak height on ice was 91% of the modeled aqueous value.
494   In terms of peak width, 1,2- and 1,4-DMOB had narrower peaks on ice, 94 and 92% of the
495   aqueous FWHM, respectively, while 1,3-DMOB had a 27% wider peak on ice. Using this
496   information, we applied the modeled peak shifts, peak height changes, and FWHM differences to
497   the measured aqueous absorbance spectrum for each compound. This results in predicted
498   absorbance spectra at the air-ice interface for each DMOB isomer, which are shown in Figure 2
499   (dashed colored lines) and in Supplemental Figure S14.

500   We also used the molecular model results to assess the relative contributions of the phenyl ring
501   and methoxy groups to the light absorbance of each DMOB. As indicated in Supplemental
502   Figure S15, small geometrical changes in the phenyl ring are primarily responsible for the shifts
503   in the absorption spectra for all three DMOB isomers, while the methoxy groups make a minor
504   contribution. Changes in the geometry of the phenyl ring are responsible for 95 - 98% of the
505   light absorbance shifts in aqueous solution and 96 - 98% at the air-ice interface. These findings
506   are consistent with our previous work on guaiacol (Bononi et al. 2020, Hullar et al. 2020).
507   Overall, these results suggest that differences in the atomic environments around the aromatic
508   ring modify its geometry and determine their vertical excitation and are the primary factor
509   controlling light absorption changes between aqueous solution and the air–ice interface.

510   As seen in Figure 2, the predicted spectrum for each isomer at the air-ice interface (dashed
511   colored line) is noticeably different than the measured aqueous spectrum (solid colored line),
512   with bathochromic peak shifts and changes in absorbance spectrum shape. To assess the impact
513   of these changes on light absorbance, for each isomer we multiplied the aqueous and air-ice
514   interface wavelength-specific molar absorption coefficientsabsorptivities by the experimental or
515   Summit photon fluxes to determine the rate constant for light absorbance at each wavelength
516   (Supplemental Figure S16). For each DMOB isomer, the rate constant for light absorbance is a
517   wavelength-specific value giving the rate at which photons are absorbed per molecule of test
518   compound for a given light condition. We then summed the wavelength-specific values to
519   obtain the overall rate constant for light absorbance in aqueous solution and at the air-ice
520   interface for each isomer, for laboratory and Summit light conditions (Supplemental Table S4).
521   Because all three isomers show bathochromic absorbance shifts at the air-ice interface relative to
522   aqueous solution, the overall rate constants for light absorption are generally higher at the air-ice
523   interface. 1,3-DMOB, which has the largest absorbance spectrum bathochromic shift (5.2 nm),
524   shows the largest change in overall light absorption, with a 5.3-fold increase relative to aqueous
525   solution for experimental light conditions; for Summit actinic flux, the rate constant of light
526   absorption increases by a factor of 170 from solution to air-ice interface. Conversely, the light
527   absorption peak for 1,4-DMOB shifts only slightly from solution to ice and has a greater overlap
528   with the photon flux curves in solution, so the rate of light absorption increases only slightly
529   (10% or less) from solution to the air-ice interface. These results show that the amount of light
530   absorbed can be dramatically affected by absorbance changes and that this effect depends
531   strongly on the position of the absorbance spectrum relative to photon fluxes and on the

532   magnitude of the absorbance shift on ice. Comparing the overall light absorbed under laboratory
533   versus Summit light conditions, 1,2-DMOB in either aqueous solution or at the air-ice interface
534   absorbs around 200 times as much light in our lab system compared to Summit, while for 1,4-
535   DMOB the light absorption is approximately equal in both systems. 1,3-DMOB presents a more
536   complex picture: in aqueous solution, the rate constant of light absorption is about 400-fold
537   greater under laboratory illumination compared to Summit light conditions, but at the air-ice
538   interface, light absorption is only 12-fold greater in the lab relative to Summit conditions due to
539   the absorbance shift on ice. For 1,2- and 1,3-DMOB, wavelengths from 275 to 295 and 295 to
540   315 nm are most photochemically important for lab and Summit light conditions, respectively;
541   for 1,4-DMOB, these ranges are 280-315 and 300-320 nm.

542   Our observed increases in photochemical degradation rates at the air-ice interface can be caused
543   by increases in light absorbance, quantum yield, or a combination of both. As shown previously
544   (Hullar et al. 2020), by solving equation (1) for quantum yield we can use the calculated
545   enhancements in the rate constant of light absorbance from our modeling results to estimate how
546   quantum yields change from solution to the air-ice interface. Using the measured aqueous and
547   predicted ice spectra for each compound, we calculated the quantum yields for each isomer
548   under various conditions (Table 1). Our experimental results suggest LLRs may represent an
549   environment different from either aqueous solution or QLLs. However, we did not model light
550   absorbance changes in LLRs, and the available literature is inconclusive on the likelihood of
551   absorbance shifts in LLRs, so for the quantum yield calculations we assumed our test compounds
552   have the same molar absorption coefficientsabsorptivities in LLRs as in aqueous solution.

553   For 1,2-DMOB, the our quantum yield in aqueous solution calculated from our experimental
554   results is 0.015 (± 0.0085, 1 σ). Because the experimental data is noisy, the calculated quantum
555   yield for frozen solution is statistically indistinguishable from zero. LN2 samples had a similar
556   quantum yield to aqueous solution, although again the quantum yield is indistinguishable from
557   zero. In both VD-to-ice and VD-to-snow samples, where we would expect to find 1,2-DMOB at
558   the air-ice interface, the quantum yields were approximately 8 times higher than in aqueous
559   solution or LLRs, and were the highest calculated for any isomer and sample type, e.g., 0.12 ±
560   0.039 in the VD-to-snow samples. For 1,3-DMOB, the negative experimental reaction rate
561   constant for loss in solution (Figure 1b) precludes calculating a quantum yield; however, using
562   the calculated confidence interval (Table 1) we can provide an upper-bound estimate of 0.016.
563   In both LN2 (LLR) and VD-to-snow (air-ice interface) sample types, the 1,3-DMOB calculated
564   quantum yields are similar, and at least 5 times higher than in aqueous solution.   For 1,4-
565   DMOB, the estimated aqueous solution quantum yield of 0.0020 (± 0.00042) is approximately 8-
566   fold less than that of 1,2-DMOB; the quantum yield in LLRs is approximately 4 times higher
567   than in aqueous solution. At the air-ice interface, the 1,4-DMOB quantum yield (0.052 ± 0.042
568   mlc photon^{-1}) had the largest increase in quantum yield relative to aqueous solution of any of the
569   isomers, approximately 26-fold. These results are in the same range as previous results showing
570   40- and 3-fold increases in air-ice interface calculated quantum yields for guaiacol and nitrate,
571   respectively (Hullar et al. 2020, 2018).

572   Next, we evaluated the relative contributions of increased light absorbance and larger quantum
573   yields to the photodegradation rate enhancements at the air-ice interface relative to solution. For
574   1,2- and 1,4-dimethoxybenzene, the faster photodegradation on ice is primarily due to an
575   increase in quantum yield. In contrast, for 1,3-DMOB the enhanced photodegradation at the air-
576   ice interface is roughly equally due to increases in quantum yield and light absorbance. As in

577 our earlier work with guaiacol (Hullar et al. 2020), light absorbance changes are never the
578 dominant factor controlling rate constant enhancements. Increased light absorption accounts for
579 16%, 49% or less, and 4% of the reactivity enhancement on snow relative to aqueous solution for
580 1,2-, 1,3-, and 1,4-DMOB, respectively. Thus, higher quantum yields account for the bulk of the
581 enhancement seen at the air-ice interface, accounting for 84%, at least 51%, and 96% of the
582 observed enhancements, respectively. These results are roughly consistent with our previous
583 observations for guaiacol, where the quantum yield increased at the air-ice interface by a factor
584 of 41, accounting for 95% of the overall 77-fold increase in reactivity compared to aqueous
585 solution (Hullar et al. 2020).

586 **3.~~3~~4 Estimated photodegradation rate constants for loss under environmental conditions and**
587 **sensitivity to absorbance shifts**

588 To assess the environmental significance of our findings, we calculated dimethoxybenzene
589 photodegradation rate constants for loss and photochemical lifetimes in each compartment for
590 Summit, Greenland conditions (Table 1). For these calculations, we used modeled actinic fluxes
591 at Summit (section 2.3) and our estimated quantum yields (section 3.~~3~~2); because our
592 computational modeling did not include LLRs, we used measured aqueous spectra to represent
593 absorbance in both aqueous and LLR compartments, and our predicted ice spectra (Figure 2) for
594 the air-ice interface. 1,2-DMOB has slow photodegradation rate constants and very long
595 photochemical lifetimes (~60 years) in solution and in LLRs. At the air-ice interface, it
596 photodegrades 13 times faster, but the resulting lifetime is still long – approximately 1800 days
597 of midday, summer solstice sunlight. Thus even with the rate constant enhancement at the
598 interface, direct photochemical degradation is still apparently negligible. Similar to 1,2-DMOB,
599 1,3-DMOB has long lifetimes and slow degradation rate constants in the aqueous and LLR
600 compartments (45,000 and 6400 days respectively; Table 1). However, because of its significant
601 bathochromic absorbance shift (5.2 nm), the lifetime of 1,3-DMOB at the air-ice interface
602 decreases to 48 days. This result suggests 1,3-DMOB persistence in the environment could
603 change significantly if present at the air-ice interface instead of in LLRs, or if its absorbance
604 spectrum in LLRs shifts bathochromically as it does at the air-ice interface. ~~, suggesting its~~
605 ~~persistence in the environment may change significantly depending on where it is found in snow~~
606 ~~or ice.~~ For 1,4-DMOB, its absorption is already at longer wavelengths compared to the other
607 two isomers, so it absorbs more light under environmental conditions and therefore can undergo
608 faster photodegradation: lifetimes are 70, 19, and 2.7 days in aqueous solution, LLRs, and QLLs,
609 respectively, under Summit conditions. These results show that the location of an impurity in a
610 snowpack can strongly influence photochemical degradation rates. For compounds that absorb
611 sunlight substantially in solution, direct photochemical reactions at the air-ice interface may be
612 an important transformation process in snowpacks. However, quantifying this effect requires
613 understanding the portion of a compound at the air-ice interface, which is poorly known.

614 As discussed above, enhanced reactivity at the air-ice interface is primarily due to increases in
615 the quantum yield, ranging from at least 5-fold (1,3-DMOB) to 41-fold (guaiacol) (Hullar et al.
616 2020). However, although we can predict absorbance shifts at the air-ice interface using
617 molecular modeling techniques, we cannot currently predict quantum yield changes using either
618 computational or experimental methods. While changes in quantum yields affect
619 photodegradation rate constants linearly – a doubling of quantum yield will double the rate
620 constant for loss – absorbance shifts cause nonlinear effects. To evaluate the impact of
621 absorbance shifts on compound photodegradation, Figure 4a shows the calculated ratios of

622   absorbance-shifted rate constants to the unshifted rate constant. We estimated environmental
623   ($j_{TUV,DMOB}$) and lab photodegradation rate constants for each isomer using our calculated aqueous
624   solution quantum yield, Summit or experimental photon fluxes, and our measured aqueous
625   absorbance including bathochromic and hypsochromic shifts to simulate absorbance changes
626   in/on ice. For our experimental photon flux, a 5 nm bathochromic shift (approximately equal to
627   the largest shift modeled for the three DMOB isomers) changes the photodegradation rate
628   constants for loss by factors of 3.1 and 2.1 for 1,2-DMOB and 1,4-DMOB respectively. A 10
629   nm shift, similar to that measured for several aniline derivatives (Corrochano et al. 2017),
630   increases the photodegradation rate constants by factors of 7.8 and 4.2. Because 1,4-DMOB
631   absorbs more strongly at longer wavelengths than 1,2-DMOB and therefore has greater initial
632   overlap with the experimental photon flux (Figure 2), shifts have a smaller impact than for 1,2-
633   DMOB. For a 5 nm hypsochromic (blue) shift, 1,2-DMOB and 1,4-DMOB rate constants are
634   reduced by factors of 0.24 and 0.46, respectively; for a 10 nm shift, the factors are 0.040 and
635   0.19. As with red shifts, 1,2-DMOB shows greater sensitivity to a blue shift than does 1,4-
636   DMOB. With Summit actinic fluxes, we see a similar pattern, but a greater sensitivity to shift
637   (Figure 4a) due to the faster increase in actinic flux with increasing wavelength for Summit
638   compared to our experimental photon fluxes (Figure 2). For 1,2-DMOB, a 10 nm red or blue
639   shift changes the rate constants by factors of 90 or 0.0078, respectively, under Summit (TUV)
640   photon fluxes. For 1,4-DMOB, the same shifts yield changes of 16- or 0.029-fold. 1,3-DMOB
641   has a very similar absorbance spectrum to 1,2-DMOB, and thus shows similar impacts of a shift
642   in its absorbance spectrum (Supplemental Figure S17). Supplemental Figure S18 compares
643   guaiacol photodegradation rate constant changes estimated using TUV actinic flux and under
644   three different experimental light source conditions from this and previous work (Hullar et al.
645   2020), showing how our experimental illumination system has been improved over time, but still
646   does not fully reproduce the solar spectrum of Summit conditions.

647

648
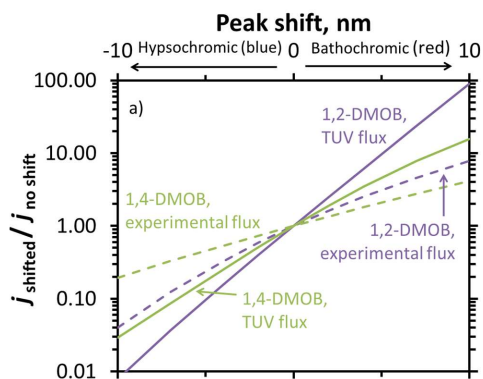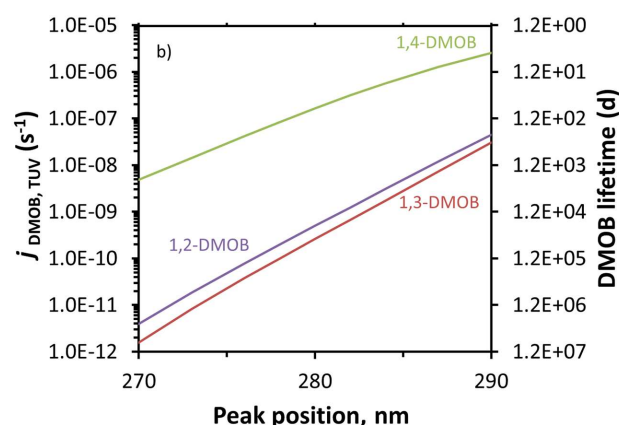
649 **Figure 4**. Predicted changes to photodegradation rate constants for loss and lifetimes resulting from
650 absorbance shifts for DMOB isomers. Rate constants for loss were determined using calculated aqueous
651 quantum yields, aqueous absorbance spectra shifted either hypsochromically (towards shorter
652 wavelengths) or bathochromically (towards longer wavelengths), and either experimental photon fluxes
653 (dashed lines) or the modeled actinic flux for Summit conditions (solid lines). a) Changes in absorbance-
654 shifted photodegradation rate constants ($j*_{DMOB}$ for experimental conditions, $j*_{DMOB,TUV}$ for TUV-modeled
655 photon fluxes) relative to unshifted values for 1,2- and 1,4-DMOB in aqueous solution. b) Estimated
656 changes in direct photodegradation rate constant ($j_{DMOB,TUV}$) and corresponding lifetime for each DMOB
657 isomer under Summit conditions for various shifts in the light absorbance peak.

658

659 While the impact of a red-shift in absorbance can be dramatic, this does not necessarily translate
660 to a short lifetime. For example, a 10-nm red shift for 1,2-DMOB increases the rate constant for
661 photodegradation by a factor of 90 (Figure 4a), but this only reduces the lifetime from 23,000 to
662 260 days (Figure 4b). 1,3-DMOB, which has essentially the same absorbance spectrum, behaves
663 similarly (Figures 4, 5, and S17). The behavior of 1,4-DMOB is different, however, since it
664 overlaps the most with the solar spectrum (Figure 2): while its rate constant for loss is less
665 sensitive to a shift in absorbance (e.g., increasing by a factor of 16 for a 10-nm red shift), this
666 changes the lifetime from 71 to 4.5 days (Figure 4b), which is short enough to be significant for
667 its environmental fate.

668 **3.~~4~~5 Sensitivity analysis of absorbance parameters on photodegradation rate constants for a**
669 **hypothetical model compound**

670 To generalize our experimental findings to other chemicals, we calculated photodegradation rate
671 constants and lifetimes for a hypothetical model compound with an assumed Gaussian
672 absorbance spectrum under Summit conditions and with a quantum yield of 1. We first ~~chose~~
673 made a single ~~hypothetical~~ absorbance curve for a hypothetical model compound, then evaluated
674 the impact of three variables: peak position, peak width, and peak height. We ~~created a single~~
675 ~~hypothetical model compound with absorbance~~ represented the model compound absorbance
676 spectrum as a Gaussian curve with its peak at 280 nm, peak height (molar absorption

677 coefficient~~absorptivity~~) of 3000 M^{-1} cm^{-1}, and a standard deviation (controlling peak width) of 7
678 nm. We derived these parameters by first fitting a Gaussian curve to each of the measured ~~These~~
679 ~~parameters were determined by fitting two Gaussian curves to the~~ absorbance spectra for 1,2-
680 and 1,4-DMOB (Supplemental Figure S19); because the right-hand (red side) of each absorbance
681 spectrum determines the amount of light absorbed, we selected curves to fit this portion of the
682 measured absorbance spectra. Finally, we averaged the parameters determined from the two
683 Gaussian curves in Supplemental Figure S19 to give the ~~, then applied the average parameters to~~
684 ~~give the~~ absorption spectrum of the hypothetical compound.

685 We then evaluated the impacts of shifting the peak position widely, by ± 20 nm, as illustrated in
686 Figure S20. As shown in Figure 5a for Summit sunlight, the impact of a shift depends on the
687 where it occurs, with the rate constant for photodegradation more sensitive at shorter
688 wavelengths. For example, hypsochromically moving a peak from 280 to 260 nm decreases the
689 rate constant by a factor of 320,000, while bathochromically moving the peak from 280 to 300
690 nm leads to a 920-fold increase in rate constant for loss. This difference is because the red shift
691 moves the absorbance spectrum towards wavelengths where some light is already being
692 absorbed. However, as discussed earlier, large increases in a rate constant do not necessarily
693 translate to significant photochemistry: lifetimes for our hypothetical compound are 2,200,000,
694 6.7, and 0.0072 days when the peak is centered at 260, 280, and 300 nm, respectively (Figure
695 5b). This sensitivity of shift impact to starting peak wavelength is shown even more clearly if
696 we consider a wider wavelength range, as shown in Figure S21. Once the compound absorbance
697 begins to significantly overlap with the actinic flux curve, additional red-shifting does not
698 dramatically increase the amount of light absorbed, slowing the rate of j_{max} increase. If we
699 assume our hypothetical compound experiences a 5 nm shift, the largest shift estimated by our
700 calculations of the three DMOB isomers, the rate constant would decrease by a factor of 0.0075
701 for a blue shift and increase by 9.2-fold for a red shift.

702

703
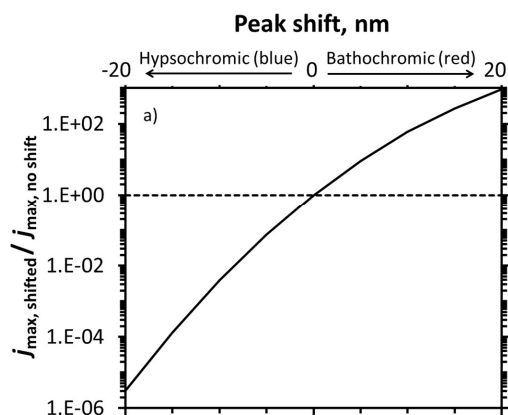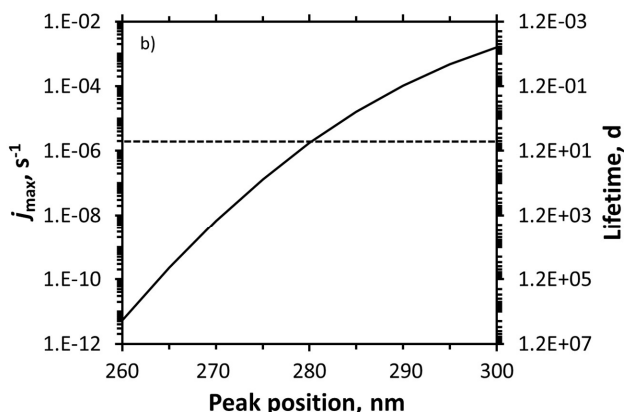
Figure 5. Predicted changes to photodegradation rate constants for loss (j_{max}) and lifetimes resulting from absorbance shifts for a hypothetical model compound. Rate constants (j_{max}) and lifetimes calculated using an assumed quantum yield of 1, modeled actinic flux for Summit conditions, and an assumed Gaussian absorbance spectrum (peak molar absorptivity 3000 M^{-1} cm^{-1}, standard deviation of 7 nm) with varying peak positions. a) Ratio of shifted to unshifted j_{max} for varying hypsochromic (blue) or bathochromic (red) absorbance shifts. b) Calculated rate constants (j_{max}) and lifetimes at various peak positions. The horizontal lines intersect the curves at the baseline peak position of 280 nm.

711

Next, we examined the impact of peak width, as illustrated in Figure S22. From our modeling, the largest peak width change was approximately 2 nm (for 1,3-DMOB). As seen in Supplemental Figure S23, narrowing the hypothetical peak from 7 to 5 nm reduces j_{max} and increases the lifetime by 88-fold, roughly 7 times larger than the lifetime decrease caused by a 5 nm hypsochromic shift of the original 7 nm wide peak. While broadening the peak to 9 nm does increase j_{max} and decrease the lifetime, the magnitude of the change is not as significant, approximately 13-fold. Similarly to the pattern seen for peak location shifts, changes in peak width cause greater impacts when the compound's absorbance peak is located at shorter wavelengths.

Finally, we evaluated the impact of changing the peak height (hyper- and hypochromic shifts). Figure S24 shows the spectra tested, and Figure S25 the results; for comparison, our largest modeled peak height change was 17%, for 1,2-DMOB. Because the area of a Gaussian curve is proportional to its peak height, doubling the height doubles the area and therefore the light absorbed would double as well. However, compared to the impact of peak location and width, even a peak height doubling exerts a relatively small influence on peak area and therefore light absorbed. To evaluate the relative impact of absorbance shifts, broadenings, and peak height (molar absorption coefficient<s>absorptivity</s>) changes on photodegradation, we assumed the largest modeled absorbance changes between aqueous solution and at the air-ice interface for the three DMOB isomers are typical for chemicals in the environment. Based on this assumption and applying these changes to our hypothetical peak, peak location and width changes at the air-ice

interface probably control overall differences in light absorption, while changes in peak height likely make a minor contribution.

4 Conclusions

Our results, together with previous studies (Hullar et al. 2020, 2007, Kahan et al. 2010, Kahan et al. 2010), suggest that for some organic compounds, QLLs and LLRs represent different photochemical reaction environments that are distinct from aqueous solution. While molecular modeling and laboratory measurements have both found evidence of absorbance shifts (Corrochano et al. 2017, Heger et al. 2005, Hullar et al. 2020, Malongwe et al. 2016), our results indicate that increases in quantum yield are the major reason for enhanced photochemical reactivity at the air-ice interface. For compounds absorbing appreciable amounts of sunlight in aqueous solution, QLL and LLR reactivity increases may cause environmentally significant changes in direct photoreaction rates and lifetimes, but for chemicals that absorb very little or no sunlight, these changes do not appear to make direct photochemistry a significant sink.

Our ability to make statistically significant conclusions depended on the choice of the experimental treatment; samples frozen in liquid nitrogen or vapor deposited to nature-identical snow provided useful insights into LLR and QLL compartments, respectively. In contrast, samples frozen in a laboratory freezer or vapor deposited to a water ice surface gave results that were noisier and less valuable. In addition, computational methods allowed us to determine absorbance spectra at the air-ice interface, where experimental observations would have been difficult.

While we find that quantum yields at the air-ice interface can be much higher than in aqueous solution, the reason for this remains unclear. Our modeling suggests small geometric changes in the configuration of the phenyl ring shifts molecular absorbance and it is possible the change in the carbon atom positions could also increase the quantum yield. Despite our use of small amounts of DMOBs deposited to the air-ice interface, which should reduce aggregation and areas of high local concentration, the observed photodegradation rate constant enhancements might be caused by higher local concentrations at the air-ice interface, increasing secondary chemistry. An additional possibility for the higher quantum yields is a weakening of the cage effect at the air ice interface. In solution (including in LLRs), the chromophore is surrounded by a cage of water molecules, which can inhibit dissociation of the excited state into products. At the air-ice interface, however, this cage will be incomplete since the molecule is exposed to air on one side. This reduced cage should increase the efficiency of the excited state decaying into products, leading to a higher quantum yield. A reduced cage effect was proposed by Meusinger et al. (2014) to possibly explain enhanced photodecay of nitrate ion in natural snow studied in the lab, although later work in Antarctica (Barbero et al. 2021) found no enhancement in nitrate quantum yield in the field.

Acknowledgments

We thank the National Science Foundation for funding (CHE 1806210 and AGS-PRF 1524857). Calculations were performed using the Extreme Science and Engineering Discovery Environment (XSEDE),[87] which is supported by the National Science Foundation, grant number ACI-154856

5. References

Abascal, J. L. F., E. Sanz, R. G. Fernandez and C. Vega: A potential model for the study of ices and amorphous water: TIP4P/Ice, Journal of Chemical Physics, 122(23), doi: 10.1063/1.1931662, 2005.

Amalric, L., C. Guillard, N. Serpone and P. Pichat: Water treatment: Degradation of dimethoxybenzenes by the titanium dioxide-UV combination, Journal of Environmental Science and Health. Part A: Environmental Science and Engineering and Toxicology, 28(6), 1393-1408, doi: 10.1080/10934529309375949, 1993.

Barbero, A., J. Savarino, R. Grilli, C. Blouzon, G. Picard, M. M. Frey, Y. Huang and N. Caillon: New Estimation of the NOx Snow-Source on the Antarctic Plateau, Journal of Geophysical Research-Atmospheres, 126(20), doi: 10.1029/2021jd035062, 2021.

Barret, M., F. Domine, S. Houdier, J. C. Gallet, P. Weibring, J. Walega, A. Fried and D. Richter: Formaldehyde in the Alaskan Arctic snowpack: Partitioning and physical processes involved in air-snow exchanges, Journal of Geophysical Research-Atmospheres, 116, doi: 10.1029/2011jd016038, 2011.

Bartels-Rausch, T., H. W. Jacobi, T. F. Kahan, J. L. Thomas, E. S. Thomson, J. P. D. Abbatt, M. Ammann, J. R. Blackford, H. Bluhm, C. Boxe, F. Domine, M. M. Frey, I. Gladich, M. I. Guzman, D. Heger, T. Huthwelker, P. Klan, W. F. Kuhs, M. H. Kuo, S. Maus, S. G. Moussa, V. F. McNeill, J. T. Newberg, J. B. C. Pettersson, M. Roeselova and J. R. Sodeau: A review of air-ice chemical and physical interactions (AICI): liquids, quasi-liquids, and solids in snow, Atmospheric Chemistry and Physics, 14(3), 1587-1633, doi: 10.5194/acp-14-1587-2014, 2014.

Bartels-Rausch, T., F. Orlando, X. R. Kong, L. Artiglia and M. Ammann: Experimental Evidence for the Formation of Solvation Shells by Soluble Species at a Nonuniform Air-Ice Interface, Acs Earth and Space Chemistry, 1(9), 572-579, doi: 10.1021/acsearthspacechem.7b00077, 2017.

Bartok, A. P., R. Kondor and G. Csanyi: On representing chemical environments, Physical Review B, 87(18), 16, doi: 10.1103/PhysRevB.87.184115, 2013.

Bononi, F. C., Z. K. Chen, D. Rocca, O. Andreussi, T. Hullar, C. Anastasio and D. Donadio: Bathochromic Shift in the UV-Visible Absorption Spectra of Phenols at Ice Surfaces: Insights from First-Principles Calculations, Journal of Physical Chemistry A, 124(44), 9288-9298, doi: 10.1021/acs.jpca.0c07038, 2020.

813 Casida, M. E., H. Chermette and D. Jacquemin: Time-dependent density-functional theory for
814 molecules and molecular solids Preface, Journal of Molecular Structure-Theochem, 914(1-3), 1-
815 2, doi: 10.1016/j.theochem.2009.08.013, 2009.

816
817 Chu, L. and C. Anastasio: Quantum yields of hydroxyl radical and nitrogen dioxide from the
818 photolysis of nitrate on ice, Journal of Physical Chemistry A, 107(45), 9594-9602, doi:
819 10.1021/jp0349132, 2003.

820
821 Chu, L. and C. Anastasio: Formation of hydroxyl radical from the photolysis of frozen hydrogen
822 peroxide, Journal of Physical Chemistry A, 109(28), 6264-6271, doi: 10.1021/jp051415f, 2005.

823
824 Chu, L. and C. Anastasio: Temperature and wavelength dependence of nitrite photolysis in
825 frozen and aqueous solutions, Environmental Science & Technology, 41(10), 3626-3632, doi:
826 10.1021/es062731q, 2007.

827
828 Corrochano, P., D. Nachtigallová and P. Klán: Photooxidation of Aniline Derivatives Can Be
829 Activated by Freezing Their Aqueous Solutions, Environmental Science & Technology, 51(23),
830 13763-13770, doi: 10.1021/acs.est.7b04510, 2017.

831
832 Cusentino, M. A., M. A. Wood and A. P. Thompson: Explicit Multielement Extension of the
833 Spectral Neighbor Analysis Potential for Chemically Complex Systems, Journal of Physical
834 Chemistry A, 124(26), 5456-5464, doi: 10.1021/acs.jpca.0c02450, 2020.

835
836 Domine, F. and P. B. Shepson: Air-snow interactions and atmospheric chemistry, Science,
837 297(5586), 1506-1510, 2002.

838
839 France, J. L., M. D. King, M. M. Frey, J. Erbland, G. Picard, S. Preunkert, A. MacArthur and J.
840 Savarino: Snow optical properties at Dome C (Concordia), Antarctica; implications for snow
841 emissions and snow chemistry of reactive nitrogen, Atmospheric Chemistry and Physics, 11(18),
842 9787-9801, doi: 10.5194/acp-11-9787-2011, 2011.

843
844 Galbavy, E. S., C. Anastasio, B. L. Lefer and S. R. Hall: Light penetration in the snowpack at
845 Summit, Greenland: Part 1 Nitrite and hydrogen peroxide photolysis, Atmospheric Environment,
846 41(24), 5077-5090, doi: 10.1016/j.atmosenv.2006.04.072, 2007.

847
848 Galbavy, E. S., K. Ram and C. Anastasio: 2-Nitrobenzaldehyde as a chemical actinometer for
849 solution and ice photochemistry, Journal of Photochemistry and Photobiology a-Chemistry,
850 209(2-3), 186-192, doi: 10.1016/j.jphotochem.2009.11.013, 2010.

851

852 Ge, X. C., I. Timrov, S. Binnie, A. Biancardi, A. Calzolari and S. Baroni: Accurate and
853 Inexpensive Prediction of the Color Optical Properties of Anthocyanins in Solution, Journal of
854 Physical Chemistry A, 119(16), 3816-3822, doi: 10.1021/acs.jpca.5b01272, 2015.

855
856 Giannozzi, P., O. Andreussi, T. Brumme, O. Bunau, M. B. Nardelli, M. Calandra, R. Car, C.
857 Cavazzoni, D. Ceresoli, M. Cococcioni, N. Colonna, I. Carnimeo, A. Dal Corso, S. de Gironcoli,
858 P. Delugas, R. A. DiStasio, A. Ferretti, A. Floris, G. Fratesi, G. Fugallo, R. Gebauer, U.
859 Gerstmann, F. Giustino, T. Gorni, J. Jia, M. Kawamura, H. Y. Ko, A. Kokalj, E. Kucukbenli, M.
860 Lazzeri, M. Marsili, N. Marzari, F. Mauri, N. L. Nguyen, H. V. Nguyen, A. Otero-de-la-Roza, L.
861 Paulatto, S. Ponce, D. Rocca, R. Sabatini, B. Santra, M. Schlipf, A. P. Seitsonen, A. Smogunov,
862 I. Timrov, T. Thonhauser, P. Umari, N. Vast, X. Wu and S. Baroni: Advanced capabilities for
863 materials modelling with QUANTUM ESPRESSO, Journal of Physics-Condensed Matter,
864 29(46), 30, doi: 10.1088/1361-648X/aa8f79, 2017.

865
866 Grabner, G., S. Monti, G. Marconi, B. Mayer, C. Klein and G. Kohler: Spectroscopic and
867 photochemical study of inclusion complexes of dimethoxybenzenes with cyclodextrins, Journal
868 of Physical Chemistry, 100(51), 20068-20075, doi: 10.1021/jp962231r, 1996.

869
870 Grabner, G., W. Rauscher, J. Zechner and N. Getoff: Photogeneration of Radical Cations from
871 Aqueous Methoxylated Benzenes, Journal of the Chemical Society-Chemical Communications,
872 (5), 222-223, doi: 10.1039/c39800000222, 1980.

873
874 Grannas, A. M., W. C. Hockaday, P. G. Hatcher, L. G. Thompson and E. Mosley-Thompson:
875 New revelations on the nature of organic matter in ice cores, Journal of Geophysical Research-
876 Atmospheres, 111(D4), doi: D04304 10.1029/2005jd006251, 2006.

877
878 Grannas, A. M., A. E. Jones, J. Dibb, M. Ammann, C. Anastasio, H. J. Beine, M. Bergin, J.
879 Bottenheim, C. S. Boxe, G. Carver, G. Chen, J. H. Crawford, F. Domine, M. M. Frey, M. I.
880 Guzman, D. E. Heard, D. Helmig, M. R. Hoffmann, R. E. Honrath, L. G. Huey, M. Hutterli, H.
881 W. Jacobi, P. Klan, B. Lefer, J. McConnell, J. Plane, R. Sander, J. Savarino, P. B. Shepson, W.
882 R. Simpson, J. R. Sodeau, R. von Glasow, R. Weller, E. W. Wolff and T. Zhu: An overview of
883 snow photochemistry: evidence, mechanisms and impacts, Atmospheric Chemistry and Physics,
884 7(16), 4329-4373, 2007.

885
886 Grimme, S., J. Antony, S. Ehrlich and H. Krieg: A consistent and accurate ab initio
887 parametrization of density functional dispersion correction (DFT-D) for the 94 elements H-Pu,
888 Journal of Chemical Physics, 132(15), 19, doi: 10.1063/1.3382344, 2010.

889
890 Hartwigsen, C., S. Goedecker and J. Hutter: Relativistic separable dual-space Gaussian
891 pseudopotentials from H to Rn, Physical Review B, 58(7), 3641-3662, doi:
892 10.1103/PhysRevB.58.3641, 1998.

893

Heger, D., J. Jirkovsky and P. Klán: Aggregation of methylene blue in frozen aqueous solutions studied by absorption spectroscopy, Journal of Physical Chemistry A, 109(30), 6702-6709, doi: 10.1021/jp050439j, 2005.

Heger, D. and P. Klán: Interactions of organic molecules at grain boundaries in ice: A solvatochromic analysis, Journal of Photochemistry and Photobiology a-Chemistry, 187(2-3), 275-284, doi: 10.1016/j.jphotochem.2006.10.012, 2007.

Hullar, T. and C. Anastasio: Direct visualization of solute locations in laboratory ice samples, Cryosphere, 10(5), 2057-2068, doi: 10.5194/tc-10-2057-2016, 2016.

Hullar, T., F. C. Bononi, Z. K. Chen, D. Magadia, O. Palmer, T. Tran, D. Rocca, O. Andreussi, D. Donadio and C. Anastasio: Photodecay of guaiacol is faster in ice, and even more rapid on ice, than in aqueous solution, Environmental Science-Processes & Impacts, 22(8), 1666-1677, doi: 10.1039/d0em00242a, 2020.

Hullar, T., D. Magadia and C. Anastasio: Photodegradation Rate Constants for Anthracene and Pyrene Are Similar in/on Ice and in Aqueous Solution, Environmental Science & Technology, 52(21), 12225-12234, doi: 10.1021/acs.est.8b02350, 2018.

Jacobi, H. W., R. C. Bales, R. E. Honrath, M. C. Peterson, J. E. Dibb, A. L. Swanson and M. R. Albert: Reactive trace gases measured in the interstitial air of surface snow at Summit, Greenland, Atmospheric Environment, 38(12), 1687-1697, doi: 10.1016/j.atmosenv.2004.01.004, 2004.

Kahan, T. F. and D. J. Donaldson: Photolysis of polycyclic aromatic hydrocarbons on water and ice surfaces, Journal of Physical Chemistry A, 111(7), 1277-1285, doi: 10.1021/jp066660t, 2007.

Kahan, T. F. and D. J. Donaldson: Benzene photolysis on ice: Implications for the fate of organic contaminants in the winter, Environmental Science & Technology, 44(10), 3819-3824, doi: 10.1021/es100448h, 2010.

Kahan, T. F., N. O. A. Kwamena and D. J. Donaldson: Different photolysis kinetics at the surface of frozen freshwater vs. frozen salt solutions, Atmospheric Chemistry and Physics, 10(22), 10917-10922, doi: 10.5194/acp-10-10917-2010, 2010.

Kahan, T. F., R. Zhao, K. B. Jumaa and D. J. Donaldson: Anthracene photolysis in aqueous solution and ice: Photon flux dependence and comparison of kinetics in bulk ice and at the air-ice interface, Environmental Science & Technology, 44(4), 1302-1306, doi: 10.1021/es9031612, 2010.

935   Kania, R., J. K. Malongwe, D. Nachtigallová, J. Krausko, I. Gladich, M. Roeselová, D. Heger
936   and P. Klán: Spectroscopic properties of benzene at the air-ice interface: A combined
937   experimental-computational approach, Journal of Physical Chemistry A, 118(35), 7535-7547,
938   doi: 10.1021/jp501094n, 2014.

939
940   Kling, T., F. Kling and D. Donadio: Structure and Dynamics of the Quasi-Liquid Layer at the
941   Surface of Ice from Molecular Simulations, Journal of Physical Chemistry C, 122(43), 24780-
942   24787, doi: 10.1021/acs.jpcc.8b07724, 2018.

943
944   Krausko, J., J. K. Malongwe, G. Bičanová, P. Klán, D. Nachtigallová and D. Heger:
945   Spectroscopic properties of naphthalene on the surface of ice grains revisited: A combined
946   experimental computational approach, Journal of Physical Chemistry A, 119(32), 8565-8578,
947   doi: 10.1021/acs.jpca.5b00941, 2015.

948
949   Leang, S. S., F. Zahariev and M. S. Gordon: Benchmarking the performance of time-dependent
950   density functional methods, Journal of Chemical Physics, 136(10), 12, doi: 10.1063/1.3689445,
951   2012.

952
953   Legrain, F., J. Carrete, A. van Roekeghem, S. Curtarolo and N. Mingo: How Chemical
954   Composition Alone Can Predict Vibrational Free Energies and Entropies of Solids, Chemistry of
955   Materials, 29(15), 6220-6227, doi: 10.1021/acs.chemmater.7b00789, 2017.

956
957   Madronich, S. and S. J. Flocke (1998). The role of solar radiation in atmospheric chemistry.
958   Handbook of Environmental Chemistry. P. Boule. Heidelberg, Springer**:** 1-26.

959
960   Malongwe, J. K., D. Nachtigallová, P. Corrochano and P. Klán: Spectroscopic properties of
961   anisole at the air-ice interface: A combined experimental-computational approach, Langmuir,
962   32(23), 5755-5764, doi: 10.1021/acs.langmuir.6b01187, 2016.

963
964   Matykiewiczová, N., R. Kurkova, J. Klanova and P. Klán: Photochemically induced nitration
965   and hydroxylation of organic aromatic compounds in the presence of nitrate or nitrite in ice,
966   Journal of Photochemistry and Photobiology a-Chemistry, 187(1), 24-32, 2007.

967
968   McFall, A. S. and C. Anastasio: Photon flux dependence on solute environment in water ices,
969   Environmental Chemistry, 13(4), 682-687, doi: http://dx.doi.org/10.1071/EN15199, 2016.

970
971   McFall, A. S., K. C. Edwards and C. Anastasio: Nitrate Photochemistry at the Air-Ice Interface
972   and in Other Ice Reservoirs, Environmental Science & Technology, 52(10), 5710-5717, doi:
973   10.1021/j.acs.est.8b00095, 2018.

974

975 Meusinger, C., T. A. Berhanu, J. Erbland, J. Savarino and M. S. Johnson: Laboratory study of
976 nitrate photolysis in Antarctic snow. I. Observed quantum yield, domain of photolysis, and
977 secondary chemistry, Journal of Chemical Physics, 140(24), doi: 10.1063/1.4882898, 2014.

978
979 Miura, M., Y. Aoki and B. Champagne: Assessment of Time-Dependent Density-Functional
980 Schemes for Computing the Oscillator Strengths of Benzene, Phenol, Aniline, and
981 Fluorobenzene, J. Chem. Phys., 127, 084103- 084117, doi: 10.1063/1.2761886, 2007.

982
983 Mosi, R., G. Z. Zhang and P. Wan: Enhanced Basicity of the 2-Position of 1,3-Dialkoxybenzenes
984 in S_1: Acid-Catalyzed Photochemical Proton Deuteron Exchange, Journal of Organic Chemistry,
985 60(2), 411-417, doi: 10.1021/jo00107a021, 1995.

986
987 Perdew, J. P., K. Burke and M. Ernzerhof: Generalized gradient approximation made simple,
988 Physical Review Letters, 77(18), 3865-3868, doi: 10.1103/PhysRevLett.77.3865, 1996.

989
990 Phillips, G. J. and W. R. Simpson: Verification of snowpack radiation transfer models using
991 actinometry, Journal of Geophysical Research-Atmospheres, 110(D8), doi: D08306
992 10.1029/2004jd005552, 2005.

993
994 Pollard, R., S. Wu, G. Z. Zhang and P. Wan: Photochemistry of Dimethoxybenzenes in Aqueous
995 Sulfuric Acid, Journal of Organic Chemistry, 58(9), 2605-2613, doi: 10.1021/jo00061a042,
996 1993.

997
998 Ram, K. and C. Anastasio: Photochemistry of phenanthrene, pyrene, and fluoranthene in ice and
999 snow, Atmospheric Environment, 43(14), 2252-2259, doi: 10.1016/j.atmosenv.2009.01.044,
1000 2009.

1001
1002 Rocca, D., R. Gebauer, Y. Saad and S. Baroni: Turbo charging time-dependent density-
1003 functional theory with Lanczos chains, Journal of Chemical Physics, 128(15), 14, doi:
1004 10.1063/1.2899649, 2008.

1005
1006 Sanchez, M. A., T. Kling, T. Ishiyama, M. J. van Zadel, P. J. Bisson, M. Mezger, M. N. Jochum,
1007 J. D. Cyran, W. J. Smit, H. J. Bakker, M. J. Shultz, A. Morita, D. Donadio, Y. Nagata, M. Bonn
1008 and E. H. G. Backus: Experimental and theoretical evidence for bilayer-by-bilayer surface
1009 melting of crystalline ice, Proceedings of the National Academy of Sciences of the United States
1010 of America, 114(2), 227-232, doi: 10.1073/pnas.1612893114, 2017.

1011
1012 Schurmann, K. and M. Lehnig: Mechanistic studies of the photochemical nitration of phenols,
1013 1,2-dimethoxybenzene and anisoles with tetranitromethane by ^{15}N CIDNP, Applied Magnetic
1014 Resonance, 18(3), 375-384, doi: 10.1007/bf03162151, 2000.

1015

Smith, D. M., T. Q. Cui, M. N. Fiddler, R. P. Pokhrel, J. D. Surratt and S. Bililign: Laboratory studies of fresh and aged biomass burning aerosol emitted from east African biomass fuels - Part 2: Chemical properties and characterization, Atmospheric Chemistry and Physics, 20(17), 10169-10191, doi: 10.5194/acp-20-10169-2020, 2020.

Tajima, S., S. Tobita and H. Shizuka: Electron transfer reaction from triplet 1,4-dimethoxybenzene to hydronium ion in aqueous solution, Journal of Physical Chemistry A, 103(31), 6097-6105, doi: 10.1021/jp990743a, 1999.

Thompson, A. P., L. P. Swiler, C. R. Trott, S. M. Foiles and G. J. Tucker: Spectral neighbor analysis method for automated generation of quantum-accurate interatomic potentials, Journal of Computational Physics, 285, 316-330, doi: 10.1016/j.jcp.2014.12.018, 2015.

Tibshirani, R.: Regression shrinkage and selection via the lasso: a retrospective, Journal of the Royal Statistical Society Series B-Statistical Methodology, 73, 273-282, doi: 10.1111/j.1467-9868.2011.00771.x, 2011.

Timrov, I., O. Andreussi, A. Biancardi, N. Marzari and S. Baroni: Self-consistent continuum solvation for optical absorption of complex molecular systems in solution, Journal of Chemical Physics, 142(3), 9, doi: 10.1063/1.4905604, 2015.

Timrov, I., M. Micciarelli, M. Rosa, A. Calzolari and S. Baroni: Multimodel Approach to the Optical Properties of Molecular Dyes in Solution, Journal of Chemical Theory and Computation, 12(9), 4423-4429, doi: 10.1021/acs.jctc.6b00417, 2016.

USEPA. (2021). "CompTox Chemicals Dashboard." from https://comptox.epa.gov/dashboard/.

VandeVondele, J., M. Krack, F. Mohamed, M. Parrinello, T. Chassaing and J. Hutter: QUICKSTEP: Fast and accurate density functional calculations using a mixed Gaussian and plane waves approach, Computer Physics Communications, 167(2), 103-128, doi: 10.1016/j.cpc.2004.12.014, 2005.

Wan, P. and P. Wu: Acid-Catalyzed ipso Photosubstitution of Alkoxy-substituted Benzenes in Aqueous Acid Solution, Journal of the Chemical Society-Chemical Communications, (11), 822-823, doi: 10.1039/c39900000822, 1990.

Zhang, G. Z., Y. J. Shi, R. Mosi, T. Ho and P. Wan: Enhanced basicity of 1,3-Dialkoxy-substituted Benzenes - Cyclophane Derivatives, Canadian Journal of Chemistry-Revue Canadienne De Chimie, 72(12), 2388-2395, doi: 10.1139/v94-305, 1994.

1056   Zhu, C. Z., B. Xiang, L. T. Chu and L. Zhu: 308 nm Photolysis of Nitric Acid in the Gas Phase,
1057   on Aluminum Surfaces, and on Ice Films, Journal of Physical Chemistry A, 114(7), 2561-2568,
1058   doi: 10.1021/jp909867a, 2010.

1059

1060